Space Sci Rev (2017) 208:17–31
DOI 10.1007/s11214-015-0227-y

Preflight Calibration Test Results for Optical Navigation Camera Telescope (ONC-T) Onboard the *Hayabusa2* Spacecraft

S. Kameda[1] · H. Suzuki[2] · T. Takamatsu[1] · Y. Cho[1] · T. Yasuda[1] · M. Yamada[3] · H. Sawada[4] · R. Honda[5] · T. Morota[6] · C. Honda[7] · M. Sato[1] · Y. Okumura[1] · K. Shibasaki[1] · S. Ikezawa[1] · S. Sugita[8]

Received: 11 August 2015 / Accepted: 25 November 2015 / Published online: 18 May 2016

Abstract The optical navigation camera telescope (ONC-T) is a telescopic framing camera with seven colors onboard the *Hayabusa2* spacecraft launched on December 3, 2014. The main objectives of this instrument are to optically navigate the spacecraft to asteroid Ryugu and to conduct multi-band mapping the asteroid. We conducted performance tests of the instrument before its installation on the spacecraft. We evaluated the dark current and bias level, obtained data on the dependency of the dark current on the temperature of the charge-coupled device (CCD). The bias level depends strongly on the temperature of the electronics package but only weakly on the CCD temperature. The dark-reference data, which is obtained simultaneously with observation data, can be used for estimation of the dark current and bias level. A long front hood is used for ONC-T to reduce the stray light at the expense of flatness in the peripheral area of the field of view (FOV). The central area in FOV has a flat sensitivity, and the limb darkening has been measured with an integrat-

✉ S. Kameda
kameda@rikkyo.ac.jp

1 Department of Physics, Rikkyo University, 3-34-1 Nishi-Ikebukuro, Toshima, Tokyo 171-8501, Japan

2 Department of Physics, Meiji University, 1-1-1, Higashi-Mita, Tama-ku, Kawasaki, Kanagawa 214-8571, Japan

3 Planetary Exploration Research Center, Chiba Institute of Technology, 2-17-1 Tsudanuma, Narashino, Chiba 275-0016, Japan

4 Japan Aerospace Exploration Agency, JAXA Space Exploration Center, HAYABUSA2 Project, 3-1-1 Yoshinodai, Chuo-ku, Sagamihara, Kanagawa 252-5210, Japan

5 Natural Sciences Cluster-Science Unit, Kochi University, 2-5-1 Akebono-cho, Kochi, Kochi 780-8520, Japan

6 Graduate School of Environmental Studies, Nagoya University, Furo-cho, Chikusa, Nagoya, Aichi 464-8601, Japan

7 Research Center for Advanced Information Science and Technology, The University of Aizu, Tsuruga, Ikkimachi, Aizuwakamatsu, Fukushima 965-8580, Japan

8 Department of Earth and Planetary Science, Graduate School of Science, University of Tokyo, 7-3-1 Hongo, Bunkyo-ku, Tokyo 113-0033, Japan

ing sphere. The ONC-T has a wheel with seven bandpass filters and a panchromatic glass window. We measured the spectral sensitivity using an integrating sphere and obtained the sensitivity of all the pixels. We also measured the point-spread function using a star simulator. Measurement results indicate that the full width at half maximum is less than two pixels for all the bandpass filters and in the temperature range expected in the mission phase except for short periods of time during touchdowns.

Keywords ONC · Visible · Multi-band imaging · Asteroid · Hayabusa2 · Ryugu

1 Introduction

The optical navigation camera (ONC) system onboard the *Hayabusa2* spacecraft comprises one telescopic camera (T) and two wide-angle cameras (W1, W2). These cameras are controlled using an electronics package (ONC-AE). The camera system is operated mainly in the asteroid-approaching phase and the mission phase. In the former phase, the ONC system is used to navigate the spacecraft to asteroid 162137 Ryugu (1999 JU_3). After the arrival, planned in 2018 (Tsuda et al. 2013), a digital terrain model will be developed based on the image data obtained with the ONC. In addition, the ONC-T has a wheel with seven bandpass filters, allowing us to obtain a global spectral map of Ryugu. The terrain model and the global spectral map are important for both characterizing the asteroid and selecting touchdown points for sampling. The visible wavelength range, covered by the ONC-T, possesses a number of key spectroscopic quantities, such as albedo, spectral slope in the UV to short visible range, and 0.7-μm absorption band, important for characterizing mineralogical and physical properties of asteroid (e.g., Rivkin et al. 2004; Sugita et al. 2013). Such mineralogical and physical properties are important for understanding the origin and evolution of the asteroid and valuable for selecting the touchdown points for sampling (Tachibana et al. 2014).

0.7-μm absorption band is one of the few unambiguous diagnostic spectroscopic features for the presence of hydrated minerals on low-albedo asteroids. Although multiple minerals, such as Fe-rich serpentine, tochilinite, and chlorite, exhibit absorption band around 0.7 μm, the fact that Fe-rich serpentine has high abundance in carbonaceous chondrites, high sensitivity to heating, and a spectral band shape most consistent with that of carbonaceous chondrites suggests that Fe-rich serpentine may be the dominant source of 0.7-μm absorption band (e.g., Hiroi and Zolensky 1999). In fact, a ground-based observation of Ryugu suggests the presence of the 0.7-μm absorption band, consistent with serpentine (Vilas 2008). Although other observations have obtained flat spectra without an absorption band in the 0.7-μm region (e.g., Moskovitz et al. 2013; Lazzaro et al. 2013), such apparent discrepancy may be due to spatial heterogeneity of the asteroid surface (Vilas 2008; Sugita et al. 2013). Thus, the detectability of 0.7-μm absorption band is important for ONC observation of this asteroid, especially for selecting touchdown points. However, because the depth of the absorption is only 3–4 % for typical CM2 chondrites, such as Murchison and Murray meteorites (Cloutis et al. 2011), we need high-accuracy calibration data in order to detect it (Kameda et al. 2015). More specifically, dark current and bias would be offset noise sources and subjected to temperature change. Stray light is another noise source. Spectral sensitivity is necessary to estimate signal level and its statistical noise. Although other spectroscopic quantities, such as albedo and the UV absorption shoulder, are also important requirements, such as signal-to-noise ratio (SNR) for their observations are much less

demanding than that for 0.7-μm absorption band. In this paper, we report the preflight calibration test results and derive the flux-calibration parameters. After discussing the design of ONC-T in Sect. 2, we discuss dark current and bias in Sect. 3.1, stray light in Sect. 3.2, spectral sensitivity in Sect. 3.3, and overall SNR in Sect. 3.4.

2 Design of ONC-T

The design of the ONC system onboard the *Hayabusa2* spacecraft is based on the similar instrument onboard the *Hayabusa* spacecraft. In this section, we describe the design of the ONC system and show the differences between the ONC onboard the *Hayabusa2* spacecraft and that onboard the *Hayabusa* spacecraft (Table 1).

The ONC-T is a telescopic charge-coupled-device (CCD) camera. The CCD image sensor is E2V CCD4720AIMO. The focal length is 121.1 mm, and the pixels are 13 μm × 13 μm in size. Thus, the angular pixel resolution is 22 arcsec/pix or 0.1 mrad/pix. The point-spread function is discussed in Sect. 3.5. For the first several months after the arrival to the asteroid, the *Hayabusa2* spacecraft will stay at the home-position (HP) altitude of 20 km (Tsuda et al. 2013). The pixel resolution is 2 m/pix from the HP. The depth of field is greater than 100 m. The pixel resolution is 10 mm/pix at an altitude of 100 m.

The CCD image sensor has 1 K × 1 K pixels, and the field of view (FOV) is 6.27° × 6.27°. Thus, 2 km × 2 km of area can be imaged with ONC-T from HP. Since the diameter of Ryugu is ∼0.87 ± 0.03 km (Müller et al. 2011), the FOV is approximately twice wider than the apparent diameter of the asteroid. At 100 m of altitude, 10 m × 10 m of area can be observed with each frame.

The ONC-T has a wheel with seven bandpass filters and a panchromatic window for the correction of the light path length (Kameda et al. 2015). The center wavelengths of the filters are 390 nm (ul-band), 480 nm (b-band), 550 nm (v-band), 589 nm (Na), 700 nm (w-band), 860 nm (x-band), and 950 nm (p-band), and the bandwidths are approximately 40, 30, 30, 10, 30, 40, and 60 nm, respectively. These filters except for 'Na' were selected based on the filters used by the Eight Color Asteroid Survey (ECAS) (Zellner et al. 1985) although the central wavelengths of both ul- and b-band have been shifted longward to be fit in the sensitive spectral range of the CCD. The transmittance of the panchromatic window (wide) is constant (∼95 %) in the spectral range of 300 to 1200 nm. Further details regarding the filters are provided in Sect. 3.3. Figure 1 shows the position of the ONC system. The line of sight of the ONC-T is along the −Z direction in the spacecraft coordinate system. The ONC-T onboard the *Hayabusa* spacecraft is located near the sampler horn, which is close to the FOV and one of the potential sources of stray light. In the *Hayabusa2* mission, the ONC-T was moved far away from the sampler horn.

3 Preflight Calibration

3.1 Dark Current and Bias

Dark current is generated by thermal electrons within the detector and depends on the operating temperature of the CCD. We evaluated the dark current and its temperature dependency. Figure 2 shows the average dark current for all pixels and the standard deviation. The dark noise can be estimated using the following equation:

$$I_d = I_{d_0} \exp(cT), \tag{1}$$

Table 1 Specification of AMICA (*Hayabusa*) and ONC-T (*Hayabusa2*)

	AMICA (*Hayabusa*)	ONC-T (*Hayabusa2*)
Effective lens aperture	15 mm	15.1 mm
Focal length	120.80 mm	121.1 mm
Field of view	5.83° × 5.69°	6.27° × 6.27° (Optical black pixels are excluded)
CCD format	1024 × 1000 pixels	1056 (H) pixel × 1024 (V) pixel (16 × 1024 pixels on both sides are Optical Black pixels)
CCD pixel size	12 μm	13 μm
Pixel resolution	20.490 arcsec	22.14 arcsec
Filters (turn-over rate)	7 narrowband and 1 wide-band (4.69 s/filter) (1 : ul, 2 : b, 3 : v, 4 : w, 5 : x, 6 : zs, 7 : p, 8 : wide)	7 narrowband and 1 wide-band (4.69 s/filter), (1 : ul, 2 : wide, 3 : v, 4 : w, 5 : x, 6 : Na, 7 : p, 8 : b)
Polarizer	4 position angle glass polarizers	N/A
Pixel sampling rate	3 MHz	3 MHz
Gain factor	∼17 e^-/DN	20.95 e^-/DN
Read-out noise	∼60 e^-	38.5 e^- (measured value)
A/D conversion	12-bit	12-bit
Full-well	70,000 e^-	91,000 e^- (measured value)
Exposure times	5.44 ms, 8.20 ms, 10.0 ms, 16.4 ms, 21.8 ms, 32.8 ms, 43.5 mn, 65.6 ms, 87.0 ms, 131 ms, 174 ms, 262 ms, 348 ms, 525 ms, 696 ms, 1.05 s, 1.39 s, 2.10 s, 2.79 s, 4.20 s, 5.57 s, 8.40 s, 11.1 s, 16.8 s, 22.3 s, 33.6 s, 44.6 s, 67.2 s, 89.1 s, 13 s, 178 s, <1 μs (for smear)	5.44 ms, 8.20 ms, 10.9 ms, 16.4 ms, 21.8 ms, 32.8 ms, 43.5 ms, 65.6 ms, 87.0 ms, 131 ms, 174 ms, 262 ms, 348 ms, 525 ms, 696 ms, 1.05 s, 1.39 s, 2.10 s, 2.79 s, 4.20 s, 5.57 s, 8.40 s, 11.1 s, 16.8 s, 22.3 s, 33.6 s, 44.6 s, 67.2 s, 89.1 s, 134 s, 178 s, 0 s (for smear)
ND filter	<9 % (measured)	28–35 %
Peripheral illumination	>90 % (designed value)	∼95 % (no hood), down to 20 % (with the effect of hood, see Fig. 10)
Image memory storage	16 frames	128 MB (62 raw frames, 124 MB for raw images and 4 MB for Optical Black) × 2 for preprocessing buffer in DE or ONC-E (no storage within ONC-T and ONC-AE)
Software pixel binning	None, 2 × 2, 4 × 4, 8 × 8	None, 2 × 2, 4 × 4, 8 × 8 (processing in DE or ONC-E)
Arithmetic operation between images in storage	Average, median, mode, sum	Average, median, mode, and four arithmetic operations (in DE or ONC-E)
Output mode	Lossless image, lossy image (indicated by Q factor), histogram, average value	Raw image, lossless image (Hirew) or lossy image (lossy version of Hirew)
The other option for A/D conversion	12-bit, 1-bit (for shape model)	12-bit, 10-bit, 8-bit (via division in DE or ONC-E)

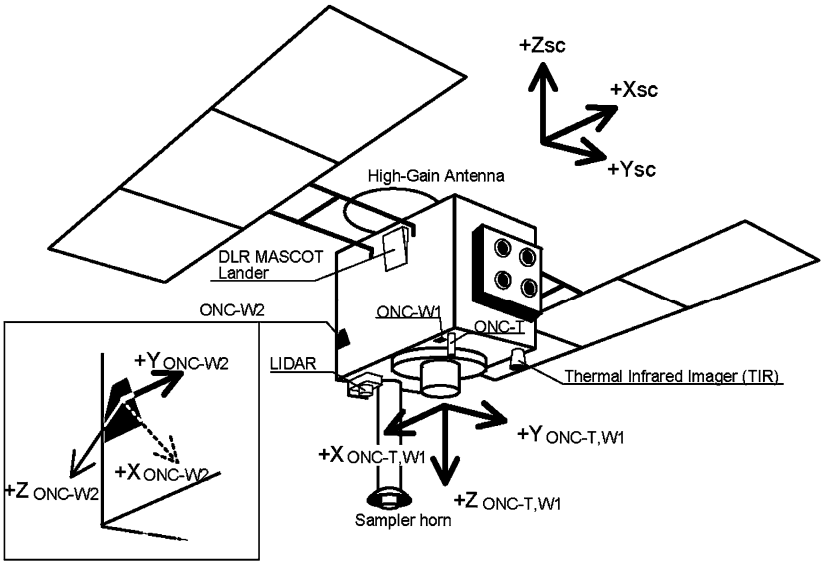

Fig. 1 A schematic three-dimensional illustration of the *Hayabusa2* spacecraft. ONC-T is located on the bottom panel. The ONC-T line of sight is in the −Z direction in the spacecraft coordinates (−Zsc)

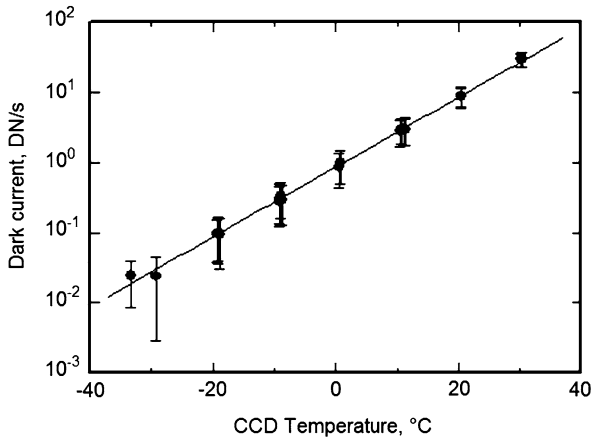

Fig. 2 Dark current and CCD temperature

where I_d is the average dark current in digital numbers (DN) per second (DN/s), I_{d_0} is the dark current in DN/s at 0 °C, T is the temperature in degrees Celsius (°C), and c is a coefficient indicating the temperature dependency of dark noise. According to our results, I_{d_0} and c are estimated to be 0.849 [DN/s] and 0.114 [°C^{-1}], respectively. ONC-T is exposed to cosmic-ray radiation, and the dark noise increases until the spacecraft arrives at the asteroid (Hopkinson 1993). We plan to obtain image data periodically to estimate the dark noise and its increase.

We also evaluated the bias (offset) level of the CCD and its temperature dependency. Figure 3 shows the average bias level for all pixels and its standard deviation and ONC-AE temperature. The bias level at an AE temperature of −30 to −20 °C is ∼100 DN higher than that at ∼+25 °C. This is probably caused by the temperature dependence of some of

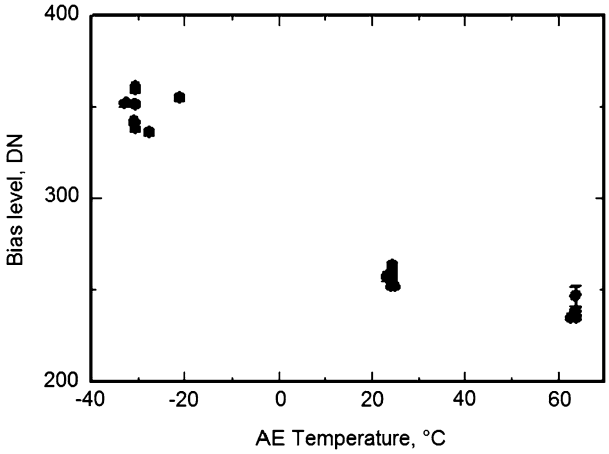

Fig. 3 Bias level and AE temperature

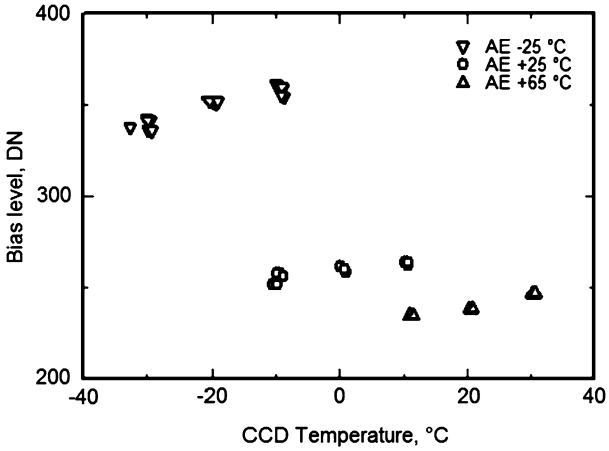

Fig. 4 Bias level and CCD temperature

the resistors used in the AE. Figure 4 shows the relationship between the bias level and CCD temperature. The bias level depends slightly on the CCD temperature. We can monitor the temperatures of the AE and CCD inflight, and we plan to save and downlink the temperature data for each set of image data. Additionally, we can use the masked regions on the CCD as a dark reference. Figure 5 shows the position of the dark-reference column.

3.2 Stray Light

In January 2013, we conducted the first optical test of the developed camera system, detecting strong stray light from the outside of the field of view. We measured the stray light at several incident angles using a telescope and a hole. The focal length of the telescope was 800 mm, and the diameter of the hole was 8 mm. The image diameter of the hole on the detector plane approximately corresponded to 80 pixels. As a result, we found that the light at an incident angle of $\sim$7.5° was scattered inside the lens tube and reached the detector surface. The intensity of the stray light was estimated as $\sim$30 % in the worst case, i.e., where the spacecraft is close to the asteroid and its apparent angular diameter is greater than $\sim$15°. We extended a front hood to block the light with an incident angle exceeding 5°

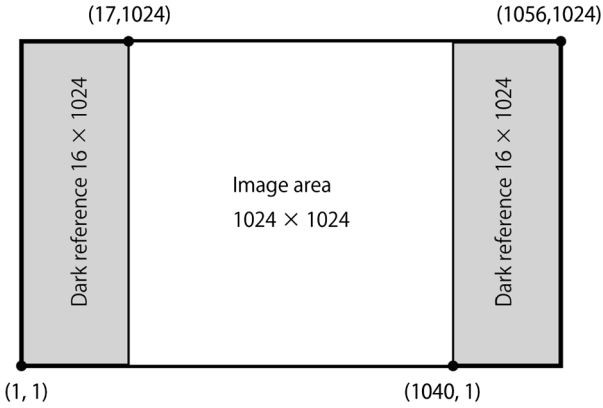

Fig. 5 *Dark-reference area* in CCD. *Gray hatched area* indicates masked regions

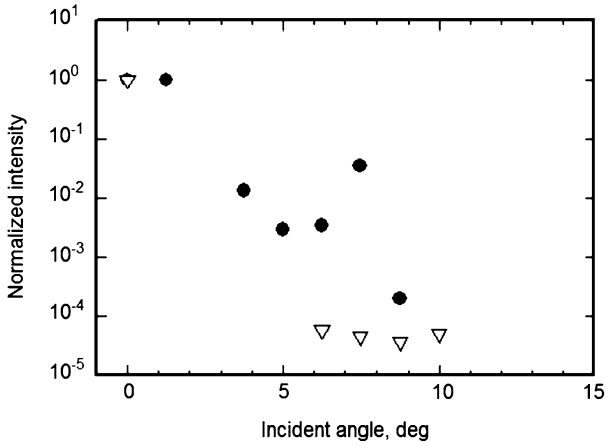

Fig. 6 Stray light intensity and incident angles before (*dot*) and after (*triangle*) modification of the front hood. The intensity is normalized at the intensity of the incident light. Note that the normalized intensities near 10^{-4} level are upper estimates because of the stray light from our measurement system

and re-manufactured a lens tube, painting the inside black. In order to ensure the stray light removal, we extended the front hood at the expense of flatness in FOV (i.e., limb darkening). Figure 6 shows the stray light and the incident angle before and after the modification. We confirmed that the stray light at an incident angle of 6–10° was successfully removed, though we did not have time to measure the stray light at an incident angle of less than 5° after modification to meet a deadline to install this instrument to the spacecraft. On the other hand, this modification caused significant limb darkening. We measured the sensitivity of each pixel using an integrating sphere, as described in Sect. 3.3. We plan to perform a flat field correction for inflight data using the measured sensitivity.

3.3 Sensitivity

The spectral sensitivity of the ONC-T camera was measured using an integrating sphere with an inner diffuse reflective coating of polytetrafluoroethylene (PTFE), an outer diameter of 12 inches (304.8 mm), and an exit aperture diameter of 5 inches (127 mm). Using four lamps, uniform illumination could be produced at the exit aperture, and the radiance could be changed by varying the lamp current. The relationship between the applied current and the spectral radiance in the aperture plane was first determined using an ideal blackbody source. The reproducibility of the radiance based on the current setting was within 0.1 %.

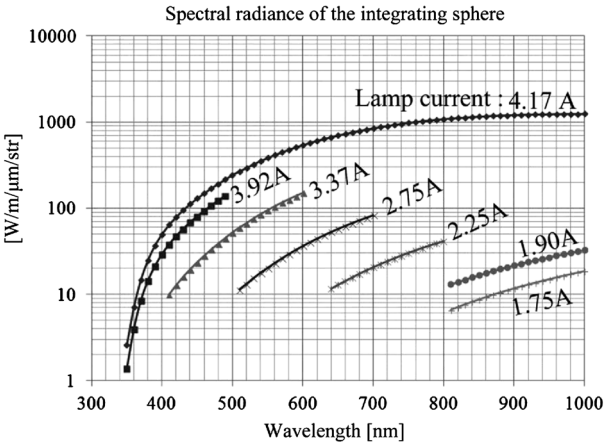

Fig. 7 Spectral radiance of the integrating sphere for different current settings

Figure 7 shows the spectral radiance of the integrating sphere for different current settings. The sensitivity of the ONC-T was calibrated by placing the camera at the aperture of the integrating sphere and obtaining images in different wavelength bands. The current settings and exposure times for each band are listed in Table 2. The current values were selected to approximately reproduce the reflected radiance from a typical asteroid at a distance of 1 AU from the Sun. Corresponding albedos lie between 3.5–6.3 % (see Table 2) for different bands since available current settings are limited for the integrating sphere. Thus, the exposure times listed in Table 2 roughly represent those required for actual asteroid imaging with an adequate signal level. During the calibration, in addition to normal images of the integrating sphere, dark images (with a shielding cap in front of the lens hood), smear images (zero exposure time without the cap), and dark bias images (zero exposure time with the cap) were recorded. Twenty five images of each type were recorded and averaged in order to reduce measurement uncertainty. The procedure used to determine the spectral sensitivity of the ONC-T is described below.

The signal level per unit exposure time, $I\,(\text{band})$, obtained from the integrating sphere is given by

$$I\,(\text{band}) = \frac{(I_R - I_{\text{smear}}) - (D - D_0)}{\tau}\ [\text{DN/s/pix}], \tag{2}$$

where I_{R}, I_{smear}, D, and D_0 are the signals associated with the normal (raw), smear, dark, and bias images, respectively. The symbol τ is the exposures time for the normal and dark images (see Table 2). As mentioned above, 25 images were successively recorded for each type of exposure and band. Thus, the mean signal level, $\overline{I}\,(\text{band})$, is given by

$$\overline{I}\,(\text{band}) = \frac{(\sum I_R - \sum I_{\text{smear}}) - (\sum D - \sum D_0)}{25\tau}\ [\text{DN/s/pix}], \tag{3}$$

where the summations are performed over 25 images.

The radiance, $I_{\text{s}}\ (\lambda_c(\text{band}))$, of the integrating sphere at the center wavelength, $\lambda_c(\text{band})$, for each band, is expressed in units of $[\text{W}/(\text{bandwidth}\,\text{m}^2)]$. Here, λ_c is given by

$$\lambda_c(\text{band}) = \frac{\sum T(\lambda)\lambda}{\sum T(\lambda)}\ [\text{nm}], \tag{4}$$

where $T(\lambda)$ is the transmittance of each bandpass filter (see Fig. 8) as a function of wavelength, and the summation is performed over all wavelengths. The bandwidth of each filter

Table 2 Current settings, exposure times, and equivalent albedos for different wavelength bands

Bands	Lamp currents of the integrating sphere [A]	Exposure times for normal images [ms]	Equivalent albedos [%]
ul	3.92	174.08	5.5
b	3.37	43.52	6.0
v	2.75	87.04	3.5
Na	2.75	131.20	5.7
w	2.25	65.60	4.7
x	1.90	65.60	6.3
p	1.75	87.04	6.3

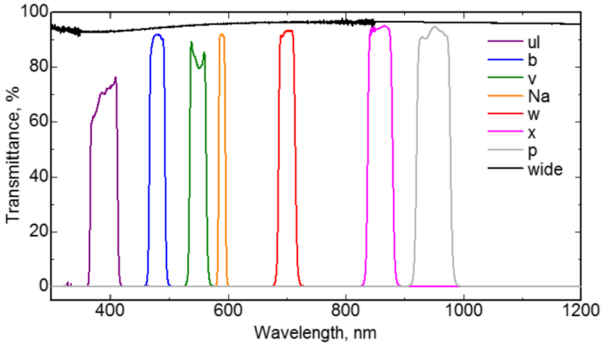

Fig. 8 Transmittance of each bandpass filter. The center wavelengths are listed in Table 3. Figure reproduced from Kameda et al. (2015)

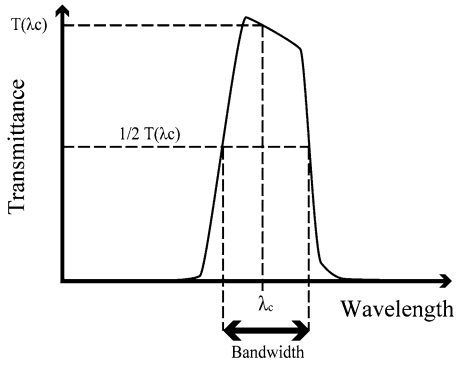

Fig. 9 Schematic of relationship between bandwidth and center wavelength

is defined as the difference between the longer and shorter wavelengths at which the transmittance of the filter becomes half of that at λ_c(band). The relationship between λ_c(band) and the bandwidth is shown schematically in Fig. 9. The calculated bandwidth and center wavelength for each filter are listed in Table 3.

Using the values given by Eqs. (3) and (4), the sensitivity in each band, $S(\lambda_c)$ is calculated by

$$S(\lambda_c) = \frac{\overline{I}(\text{band})}{\int_{\text{bandwidth}} I_s(\lambda)\, d\lambda}\ [\text{DN/s}]/\left[\text{W}/\left(\text{bandwidth}\,\text{m}^2\right)\right], \tag{5}$$

Table 3 Calculated bandwidth and center wavelength (λ_c) for each band

Bands	λ_c [nm]/bandwidth [nm]
ul	390.413/45
b	479.773/25
v	549.020/28
Na	590.160/10
w	700.384/28
x	858.947/42
p	949.697/57

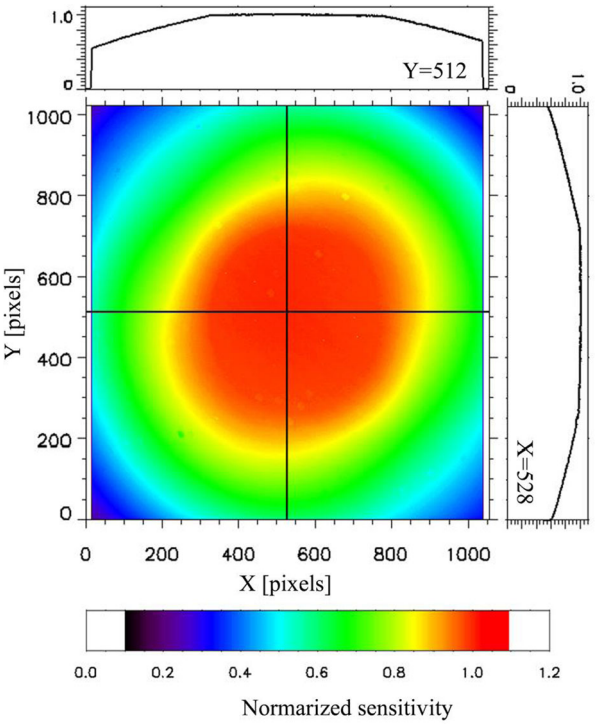

Fig. 10 Sensitivity in the v-band for all pixels

where $I_s(\lambda)$ is the known spectral radiance of the integrating sphere [W/(nm m^2)]. Figure 10 shows the calculated sensitivity in the v-band for all pixels. These values are normalized by the averaged sensitivity shown in Fig. 11 and listed in Table 4. The sensitivity profiles along $X = 528$ and $Y = 512$ lines are also indicated. The sensitivity is almost uniform near the center of the FOV and gradually decreases towards the edges, mainly due to limb darkening caused by the front hood. Similar sensitivity distributions were obtained for the other bands (not shown in this paper). It should be noted that these sensitivity distributions are very different from those for the AMICA camera onboard the *Hayabusa* spacecraft (Ishiguro et al. 2010) due to a difference in the length of the front hood. Figure 11 shows the spectral sensitivity versus λ_c for all bands except for 'wide'. These values are averaged using data for 50 pixels in the center of the FOV. The vertical dotted lines indicate the bandwidth for each band shown in Table 3. The shape of the sensitivity curve reflects well the quantum

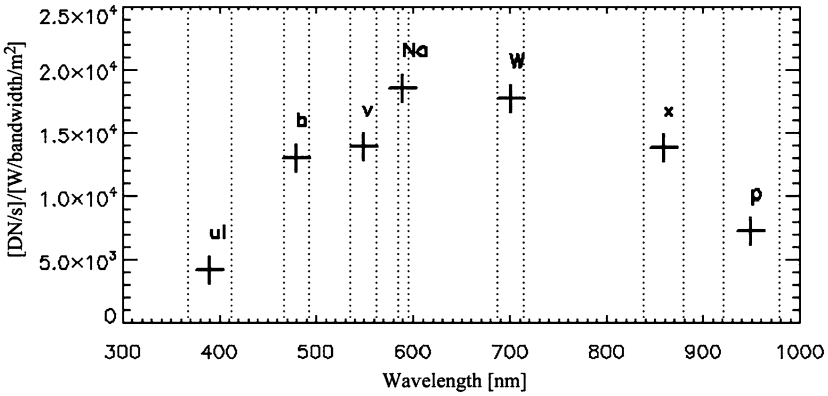

Fig. 11 Spectral sensitivity for all bands except wide-band. These values are averaged using data from 50 pixels in the center of the FOV. *The vertical dotted lines* indicate the bandwidth for each band (see Table 3)

Table 4 Sensitivities plotted in Fig. 11 together with measurement errors

Bands	λ_c [nm]	Sensitivity [DN/s]/[W/m^2/bandwidth]
ul	390.413	4177.34 ± 0.04
b	479.773	12970.7 ± 0.2
v	549.020	13859.0 ± 0.2
Na	590.106	18554.1 ± 0.2
w	700.384	17657.9 ± 0.2
x	858.947	13807.2 ± 0.2
p	949.697	7243.47 ± 0.09

efficiency of the CCD and the maximum transmittance of each bandpass filter. The average sensitivities in Fig. 11 are also listed in Table 4 together with the measurements errors. By combining these calibration values, the sensitivity distribution for all pixels (e.g., Fig. 10), and the known solar spectrum, the absolute reflectivity of asteroids can be determined from images acquired in orbit.

3.4 Estimate of Signal to Noise Ratio

As mentioned in Sect. 1, one of our spectral-mapping targets is the 0.7-μm absorption band associated with hydrated mineral(s) on Ryugu. Because the expected depth of the absorption is only 3–4 %, a very high signal-to-noise ratio (SNR) ($\geq$122) is required for detecting this absorption band with 3σ confidence level, particularly for imaging in the v-, w- and x-bands (Kameda et al. 2015). Such a high SNR requires a CCD to have high sensitivity to reduce shot noise because exposure time is limited by the surface motion due to asteroid spin. Thus, we examine whether the measured sensitivity (see Fig. 11 and Table 4) satisfies the requirement. Since it is sufficient to consider only the most insensitive band, the sensitivity in the x-band is validated here. The measured sensitivity in the x-band is 1.38×10^4 [DN/s]/[W/m^2/bandwidth] (see Table 4). The expected flux from typical asteroid with a surface albedo of 0.03 at a distance of 1.2 AU from the Sun at a wavelength of 860 nm ($\sim\lambda_c$ for the x-band) is given by $S(860\ \text{nm}) = 2.1 \times 10^{-2}$ [W/m^2/nm]. Thus, the x-band flux is $S(860\ \text{nm}) \times \text{bandwidth} = 2.1 \times 10^{-2}$ [W/m^2/nm] $\times$ 42 [nm] =

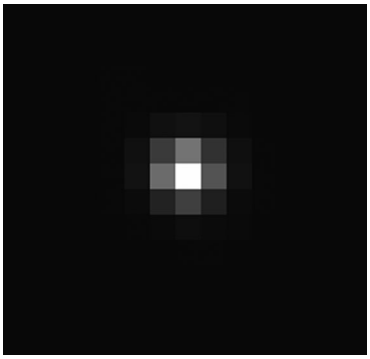

Fig. 12 An image of a point source

0.88 [W/m^2/bandwidth]. The expected signal (DN) per unit exposure time is estimated as 1.38×10^4 [DN/s]/[W/m^2/bandwidth] $\times$ 0.88 [W/m^2/bandwidth] $= 1.2 \times 10^4$ [DN/s]. Since the dynamic range for the data is 12 bits (4096 DN) for each pixel (see Table 1), the exposure time required to obtain an image of the asteroid without saturation is less than 264 ms in the present case (for available ONC-T exposure times, see Table 1). If an exposure time of 264 ms is chosen for asteroid imaging, the expected signal is 1.2×10^4 DN/s $\times$ 0.264 s $=$ 3168 DN. This digital signal can be converted to the numbers of photo-electrons produced in the CCD using the gain factor (=20.95 e$^-$/DN) to give 3168 DN $\times$ 20.95 e$^-$/DN $= 6.637 \times 10^4$ e$^-$. The total noise including shot noises, read-out noises, dark noises, and digitization noises is estimated to be 262 e$^-$. Thus, the expected SNR for an asteroid image captured with an exposure time of 264 ms is 255 (SNR $= 6.637 \times 10^4$ e$^-$/262 e$^-$) for the x-band, satisfying the minimum requirement of 122 for 0.7-μm absorption detection. For 264 ms of exposure time, surface motion due to asteroid spin is low small enough to ignore. For example, if the Müller model is assumed for the rotational period (7.63 ± 01 h) of Ryugu (Müller et al. 2011), the amount of image drift due to asteroid rotation is less than the pixel resolution (22.14 arcsec) from the Home Position of *Hayabusa2* for exposure times of up to 525 ms; no loss in spatial resolution is expected.

3.5 Point-Spread Function

The point-spread function (PSF) describes the distribution of light on the detector plane for a point source. It is affected by the optical aberration and depends on the incident angle, temperature, and wavelength. We measured the PSFs at the center and corners on the detector plane and at low and high temperatures during the thermal-vacuum tests using a star simulator comprising a telescope and a pinhole. The focal length of the telescope was 800 mm, and the diameter of the pinhole was 50 μm. The spot image diameter on the detector plane corresponded to a half pixel.

Figure 12 shows an image of a point source in the v-band. We obtained the PSFs at the center and four corners at room temperature. These positions are shown in Fig. 13. The full widths at half maximum (FWHMs) are listed in Table 5. We calculated the FWHM at a sub-pixel resolution using the results of a two-dimensional Gaussian fitting. The results indicate that the FWHM was less than 2 pixels in the entire field of view. Table 6 shows the FWHMs for the bandpass filters at the center of the detector. The FWHMs for all the filters were less than 2 pixels because of the achromatic design of the optics.

Table 7 shows the FWHMs for the v-band and the temperature of the reference point near the mounting point. The optics part was temperature-controlled by a heater in the range

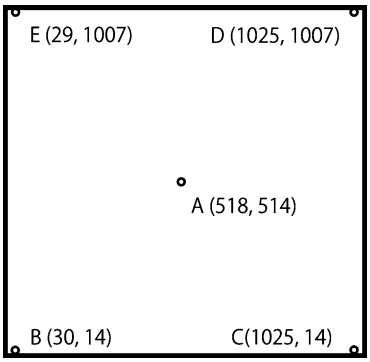

Fig. 13 Positions where PSFs were measured

Table 5 FWHM of PSF at the center and corners

Position	FWHM [pix]
A (518, 514)	1.87
B (30,14)	1.85
C (1025,14)	1.83
D (1025, 1007)	1.93
E (29,1008)	1.86

Table 6 FWHMs of PSFs with bandpass filters

Filter	FWHM [pix]
wide	1.71
ul	1.81
b	1.75
v	1.78
Na	1.72
w	1.51
x	1.56
p	1.49

Table 7 PSF and temperature

Temperature [°C]	FWHM [pix]
−25	1.87
23	1.94
55	2.57

between 10 and 40 °C. At room temperature (25 °C) and a low temperature (−25 °C), the FWHMs were less than 2 pixels. The lowest temperature in the cruising and rendezvous phase is assumed to be −25 °C. At 55 °C, the FWHM was greater than 2 pixels because the temperature of the optics went beyond the condition for which the performance was assured. Only in the descending phase for touchdowns, the temperature will increase to or beyond 25 °C. Thermal mathematical calculations indicated that the temperature at an altitude of 100 m should be less than 25 °C. These test results indicate that ONC-T optics can function

well during all the mission phases except for short periods of time during touchdowns and that the temperature history should be recorded especially in the descending phase.

4 Summary

The ONC-T onboard the *Hayabusa2* spacecraft is a multi-band framing camera similar in basic design to that onboard the *Hayabusa* spacecraft but different in details (see Sect. 2 and Table 1). We performed calibration tests on the ONC-T to measure the bias and dark currents, stray light, the FOV flatness, sensitivity, and point-spread function. We extended the front hood in order to block stray light, at the expense of flatness (i.e., limb darkening). Thus, the preflight calibration data obtained using an integrating sphere will be particularly important because of the need for flat-field correction to remove the limb darkening. We confirmed that the SNR is high enough for detection of the 0.7-μm absorption band, which is one of the few unambiguous diagnostic spectroscopic features for the presence of hydrated minerals on low-albedo asteroids. After launch, inflight calibration tests will be conducted, especially for sensitivity and dark current. The camera performances will be degraded because of the cosmic-ray irradiation in the long cruising phase. Both the preflight and inflight calibration data are indispensable for reducing the asteroid observation data.

Acknowledgements The authors wish to thank Dr. S. Nakazawa, Dr. Y. Tsuda, Dr. K. Ogawa, and *Hayabusa2* team for supporting our calibration test. The authors also wish to thank Dr. Y. Iijima for supporting our activities.

References

E.A. Cloutis, P. Hudon, T. Hiroi et al., Spectral reflectance properties of carbonaceous chondrites: 2. CM chondrites. Icarus **216**, 309 (2011). doi:10.1016/j.icarus.2011.09.009

T. Hiroi, M.E. Zolensky, UV-Vis-NIR absorption features of heated phyllosilicates as remote-sensing clues of thermal histories of primitive asteroids. Antarct. Meteor. Res. **12**, 108–116 (1999)

G.R. Hopkinson, Radiation-induced dark current increases in CCD, in *RADiation Effects on Components and Systems (RADECS)* (1993). doi:10.1109/RADECS.1993.316569

M. Ishiguro, R. Nakamura, D.J. Tholen et al., The Hayabusa spacecraft Asteroid Multi-band Imaging Camera (AMICA). Icarus **207**, 714 (2010). doi:10.1016/j.icarus.2009.12.035

S. Kameda, H. Suzuki, Y. Cho et al., Detectability of hydrous minerals using ONC-T camera onboard the Hayabusa2 spacecraft. Adv. Space Res. **56**, 1519–1524 (2015)

D. Lazzaro, M.A. Barucci, D. Perna, F.L. Jasmim, M. Yoshikawa, J.M.F. Carvano, Rotational spectra of (162173) 1999 JU3, the target of the Hayabusa2 mission. Astron. Astrophys. **549**, L2 (2013)

N.A. Moskovitz, S. Abe, K.S. Pan, D.J. Osip, D. Pefkou, M.D. Melita, M. Elias, K. Kitazato, S.J. Bus, F.E. Demeo, R.O. Binzel, O.P.A. Abell, Rotational characterization of Hayabusa II target asteroid (162173) 1999 JU3. Icarus **224**, 24 (2013)

T.G. Müller, J. Ďurech, S. Hasegawa et al., Thermo-physical properties of 162173 (1999 JU3), a potential flyby and rendezvous target for interplanetary missions. Astron. Astrophys. **525**, A145 (2011). doi:10.1501/0004-6361/201015599

A.S. Rivkin, E.S. Howell, F. Vilas, L.A. Lebofsky, Hydrated minerals on asteroids: the astronomical record, in *Asteroids III*, ed. by W. Bottke, A. Cellino, P. Paolicchi, R.P. Binzel (University of Arizona Press, Tucson, 2004), pp. 235–253

S. Sugita, T. Morota, S. Kameda, R. Honda, C. Honda, Hayabusa-2 ONC Science Team, Science observations strategy for HAYABUSA-2 optical navigation cameras (ONC), in *Lunar Planet. Sci. Conf.*, vol. XXXXIII, #3026 (2013), p. 2

S. Tachibana, M. Abe, M. Arakawa, M. Fujimoto, Y. Iijima, M. Ishiguro, K. Kitazato, N. Kobayashi, N. Namiki, T. Okada, R. Okazaki, H. Sawada, S. Sugita, Y. Takano, S. Tanaka, S. Watanabe, M. Yoshikawa, H. Kuninaka, The HAYABUSA2 Project TEAM, Hayabusa2: scientific importance of samples returned from C-type near-earth asteroid (162173) 1999 JU_3. Geochem. J. **48**, 571 (2014)

Y. Tsuda, M. Yoshikawa, M. Abe et al., System design of the Hayabusa 2—asteroid sample return mission to 1999 JU3. Acta Astronaut. **91**, 356 (2013). doi:10.1016/j.actaastro.2013.06.028

F. Vilas, Spectral characteristics of Hayabusa 2 near-Earth asteroid targets 162173 1999 JU3 and 2001 QC34. Astron. J. **135**, 1101 (2008). doi:10.1088/0004-6256/135/4/1101

F. Zellner, D.J. Tholen, E.F. Tedesco, The eight-color asteroid survey: results for 589 minor planets. Icarus **61**, 1355 (1985)